# Addressing Individual Persistent Current Switches with a Cryogenic Optical Scanner

Avirup Roy, Jonathan W. Dean, Nathan J. Ortiz, Paul Szypryt, Daniel S. Swetz, Joel C. Weber, Galen C. O'Neil

***Abstract*—We demonstrate a robust and minimalist implementation of individually addressable optically actuated persistent current switches. We use a focused laser beam directed by a cryogenic laser scanner to drive a selected segment of a superconducting loop normal with a pulse of light. We address six distinct switches with a single electrical bias, and use SQUID readout to show that persistent current is trapped successfully. Based on the cryogenic scanner's performance, we argue that this method can address over 60,000 switches, with the full array being set in about one second. Persistent current switches are widely used in quantum circuits, and we expect the ability to set tens of thousands of persistent currents with a single bias line will be useful in many applications.**

***Index Terms*—persistent current, laser scanner**

## I. Introduction

SUPERCONDUCTING circuits can make use of persistent currents—circulating currents that remain with no external bias. Any flux or current bias that is stable and non-dissipative may, in principle, be set with a persistent current switch. For example, flux biases are used to define the operating point of SQUIDs [1], the frequency and coupling of qubits [2], [3], the coupling coefficients in quantum annealers [4], synaptic weights in neuromorphic computers [5], and the gain in metallic magnetic calorimeters [6] or $\lambda$-SQUIDs [7]. Similarly, current biases are used in the operation of quantum-limited Josephson and kinetic inductance traveling wave parametric amplifiers [8]–[11] and for setting the responsivity and resonant frequency of kinetic inductance current sensors [12]. In many of these cases, it is desirable to operate systems consisting of hundreds or more devices, and it may be necessary to set one or more biases individually for each device. Here we demonstrate a method capable of setting more than 60,000 persistent current or flux biases with a single current bias line. The capability to easily set a large number of persistent current or flux biases will be useful in many large-scale superconducting and quantum systems.

Conventional implementations of persistent current switches rely on integrated resistive heaters or the use of multiple superconducting materials with different critical temperatures ($T_\mathrm{c}$). In the case of the resistive heater [13], [14], passing a current through the heater raises the temperature of a nearby superconductor above $T_\mathrm{c}$, thereby introducing a temporary resistive section. This enables flux to enter or exit the loop before the system is cooled back into the superconducting state. In the case of a material with different $T_\mathrm{c}$ sections, the temperature of a stage in a cryostat is first reduced below the transition temperature of the majority of the circuit. A current bias is applied, and then the temperature is reduced further to cause more of the circuit to superconduct and trap persistent current. Recently, four distinct persistent currents have been trapped with a single current bias [15] by generating multiple transition temperatures using the thickness dependence of the $T_\mathrm{c}$ of aluminum. Those four persistent current switches were used to precisely control the resonant frequency of four superconducting resonators to create perfect frequency spacing for multiplexed current readout. This shows one example of the power of having many individually addressable persistent current switches.

The use of a focused laser beam to deliver energy directly to the superconducting switch element provides a galvanically isolated, non-contact mechanism for inducing resistive transitions. First demonstrated in the 1970s [16], this concept was later developed for high-speed switches and inductance modulators [17], [18]. This approach significantly reduces the number of electrical interconnects entering the cryostat, minimizing parasitic heat loads, simplifying the overall system architecture, and requiring minimal space in a superconducting integrated circuit. Moreover, optical addressing offers high spatial resolution ($< 50\,\mu\mathrm{m}$) and the potential

This work was performed under financial assistance award 70NANB23H027 from the U.S. Department of Commerce, National Institute of Standards and Technology. It was also supported by NASA under Award No. 80NSSC25K7636. *(Corresponding author: P. Szypryt)*

A. Roy (email: avro2473@colorado.edu), J. W. Dean (email: jonathan.dean@nist.gov), P. Szypryt (email: paul.szypryt@colorado.edu), and J. C. Weber (email: jcweber@colorado.edu) are with the Department of Physics, University of Colorado Boulder, Boulder, CO 80309 USA.

N. J. Ortiz (email: nathan.ortiz@nist.gov), D. S. Swetz (email: daniel.swetz@nist.gov), and G. C. O'Neil (email: galen.oneil@nist.gov) are with the National Institute of Standards and Technology, Boulder, CO 80305 USA.

Color versions of one or more of the figures in this article are available online at http://ieeexplore.ieee.org

for fast modulation, making it ideally suited for dense arrays [19]–[21].

Building on earlier demonstrations of capacitive micro-electro-mechanical system (MEMS) mirror–based laser scanning [22], we employ a cryogenic optical scanner to scan a laser spot across a superconducting integrated circuit and selectively drive portions of the circuit normal. We show the trapping of persistent current actuated by optical pulses generated at room temperature, and we show that we can address one of many persistent current loops arbitrarily based on the coordinates of the scanner. Here, the superconducting element is a membrane-suspended device with $T_c \approx 50\,\mathrm{mK}$ that requires $\lesssim 5\,\mathrm{pW}$ to drive normal [23]. This device was originally designed as a transition-edge sensor (TES) microcalorimeter [24], [25]; we used an alternate bias circuit to enable the trapping of persistent current. While here we use a device with very low activation power, we predict that with a modest amount of optical power, one can drive many thin-film superconducting traces normal without modification. We demonstrate the operation of these individually addressable optically actuated switches, describe the principles of operation, and estimate that this laser scanner and optical system could individually address over 60,000 switches in $1\,\mathrm{second}$ and that with some materials a switch could be modulated at speeds of at least $3\,\mathrm{MHz}$.

## II. Experiment

To demonstrate an optically-actuated switch, we created a parallel inductor circuit where one branch could be made resistive with a laser. For this proof-of-concept, we conveniently implemented this by modifying the bias circuits of six Mo / Au bilayer detectors within a $4 \times 6$ array that we originally designed for soft X-ray microcalorimetry [23]. In their standard configuration, these devices are voltage-biased through a shunt resistor to stabilize them within their superconducting transition. To create each switch, we bypassed this resistor with a $\sim 3\,\mathrm{mm}$ long, $25\,\mu\mathrm{m}$ diameter aluminum wire bond, which forms the shunting inductor, $L_1 \approx 3.6\,\mathrm{nH}$. The current in the switch is measured by a SQUID amplifier that is flux-coupled to a $75\,\mathrm{nH}$ gradiometric inductor ($L_2$) in series with the superconducting switch element. The SQUID signals are read out with microwave SQUID multiplexing [26].

The device array is housed in a detector box mounted to the end of a $30\,\mathrm{cm}$ long, magnetically shielded, gold-plated copper "scepter" that is bolted to the mixing chamber stage of a dilution refrigerator (DR). The temperature at the end of the scepter is regulated at $24\,\mathrm{mK}$. At this temperature, well below the critical temperatures of the switch, the entire circuit becomes a superconducting loop, allowing it to support a persistent current.

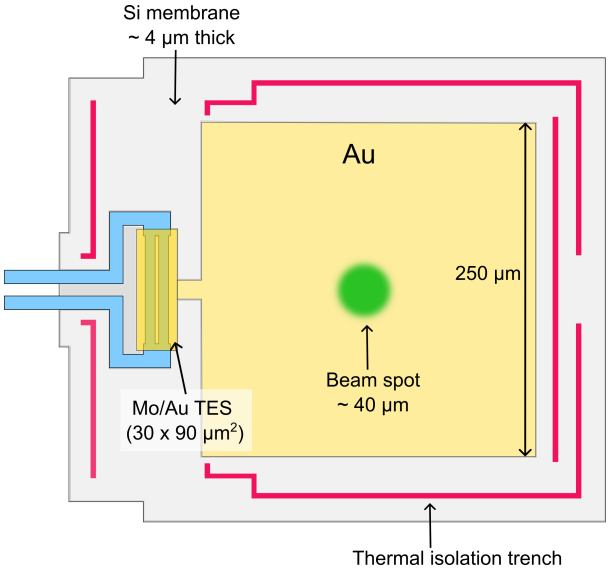


Fig. 1. Schematic of the optically actuated switch element. The Mo/Au bilayer serves as the thermally switchable element, heated by a focused 515 nm laser beam (shown in green). The jagged outermost boundary represents the outline of back etch which defines the Si membrane. The suspended membrane structure provides thermal isolation, enabling switching with only 5 pW optical power. Current through the switch is monitored via flux coupling to a gradiometric pickup inductor read out by a SQUID amplifier.

Optical control of the switches is achieved using a focused green laser ($515\,\mathrm{nm}$) with a spot size of approximately $40\,\mu\mathrm{m}$ (see Fig. 1). The power was delivered through a fiber optic chain composed of multi-mode fiber ($200\,\mu\mathrm{m}$ core diameter) running to the mixing chamber plate of the DR, followed by a final segment of single-mode fiber (mode-filled diameter $\approx 2.5\,\mu\mathrm{m}$) to the device stage. Significant coupling loss ($\sim -32\,\mathrm{dB}$) was measured at the connection between the two fiber types due to this large mode-field mismatch, but the incident beam power at the device was about $60\,\mathrm{nW}$, which is over four orders of magnitude above the $\sim 5\,\mathrm{pW}$ required to drive the switch normal.

The beam is steered by a $5\,\mathrm{mm}$-diameter aluminum-coated silicon disc bonded to a two-axis MEMS. This MEMS mirror can scan the beam across a $4\,\mathrm{cm}^2$ area, which is sufficient to address all switches in the array optically. The MEMS is electrostatically actuated and dissipates less than $300\,\mathrm{nW}$ when operating at $24\,\mathrm{mK}$. The DR has a cooling power of $\sim 2.5\,\mu\mathrm{W}$ at this temperature, so we have mounted the MEMS mirror directly to the detector box, which permits simple optics and a light-tight environment. A detailed description of the custom cryogenic laser scanning apparatus is provided in Dean *et al.* [27].

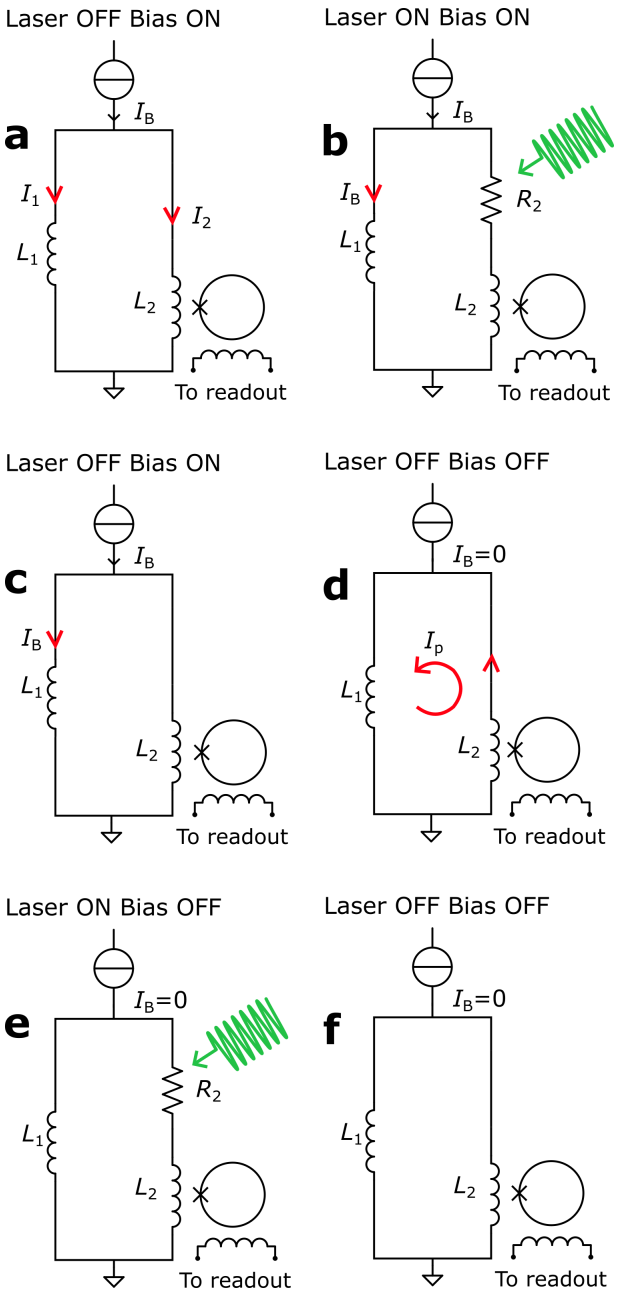


Fig. 2. The six-stage operational principle of the optical switch. **(a)** A bias current ($I_\mathrm{B}$) is applied, dividing between the two superconducting branches. **(b)** A laser pulse makes the switch resistive ($R_2$), shunting the full bias current into the $L_1$ branch. **(c)** The laser turns off and the switch cools, "freezing" the magnetic flux while the current distribution remains the same. **(d)** The external bias is removed ($I_\mathrm{B} = 0$), inducing a persistent current ($I_\mathrm{p}$) to conserve the trapped flux. **(e)** A final laser pulse opens the switch, erasing the current. **(f)** The cycle ends with zero current in the loop.

## III. Results

The operation of the persistent current switch is described by the six steps in Fig. 2. First, an external bias current, $I_\mathrm{B}$, is applied while the switch is superconducting. This current divides between the parallel branches, with the current in the switch branch given by $I_2 = I_\mathrm{B}L_1/(L_1 + L_2)$. Next, a 1 µs-wide laser pulse heats the switch above its critical temperature, turning it into a resistor, $R_2$. This shunts the entire bias current into the other branch, setting $I_1 = I_\mathrm{B}$ and forcing the switch current $I_2$ to zero. As the switch cools and becomes superconducting again, the magnetic flux from the shunted current, $\Phi = L_1 I_\mathrm{B}$, is frozen in the superconducting loop. Finally, the external bias is removed. To conserve the trapped flux, the loop induces a persistent circulating current, $I_\mathrm{p}$. As derived from flux conservation, the final value of this persistent current is $I_\mathrm{p} = -I_\mathrm{B}L_1/(L_1 + L_2)$, which is equal and opposite to the initial switch current, $I_2$. A final reset step can be performed by firing the laser with no bias to erase the stored current.

### A. Individual Switch Addressing

A bias current $I_\mathrm{B} = 153\,\mu\mathrm{A}$ is generated from a $300\,\mathrm{mV}$ source across a $1952\,\Omega$ bias resistor and applied to the parallel inductors $L_1 = 3.6\,\mathrm{nH}$ and $L_2 = 75\,\mathrm{nH}$ generating $I_2 \approx 6\,\mu\mathrm{A}$. We expect significant variation from switch to switch due to the use of wire bonds of different lengths to set $L_1$. We have measured the normal resistance of the switch $R_2 \sim 7\,\mathrm{m}\Omega$, so the relevant switching time is $(L_1 + L_2)/R_2 \approx 11\,\mu\mathrm{s}$. Fig. 3 shows data from six switches on the detector chip. The bias current is set by a square wave with 50% duty cycle and 100 ms period, while the laser pulses are generated at 50 ms period. In the first panel, the laser scanner is set to the position to activate the first switch, and only the first switch has trapped current. In each other panel the laser scanner is moved to activate a different switch, and only that switch shows trapped current. This demonstrates the ability to independently set the value of current in each switch.

For a perfect switch, the trapped current after removing the bias would be exactly equal and opposite to the current before the first laser pulse in Fig. 3. Taking the root-mean-square (RMS) value of the set and the trapped currents for each switch, we find the mean difference across the six devices tested here is $(0.23 \pm 0.15)\%$, with a median difference of 0.19%.

## IV. Scalability and Addressing Speed

One key advantage of this optical control architecture is its immense scalability. The number of persistent current switches that can be addressed is limited only

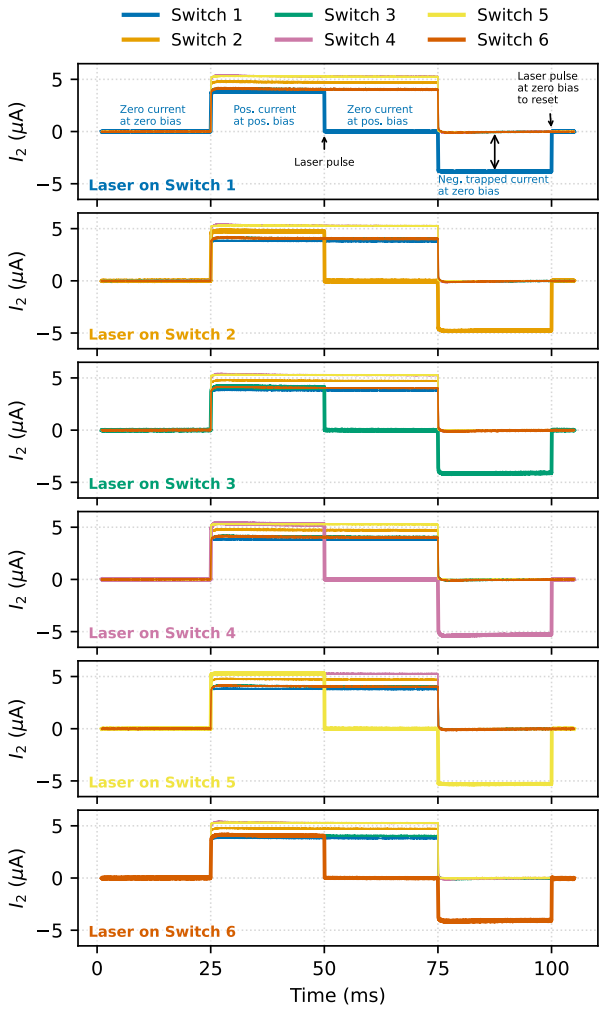


Fig. 3. Demonstration of selective optical addressing of six persistent current switches. Each panel shows the result of a write-erase cycle on a single targeted channel (e.g., Switch 1 in the top panel). At $t = 0$, a 1 µs-wide laser pulse resets all switches to zero current. A positive bias current is applied to all channels from 25 ms to 75 ms. At $t = 50$ ms a laser pulse makes the targeted switch resistive, shunting its current to zero. When the bias is turned off at 75 ms, a negative persistent current is stored in the targeted channel, equal and opposite to the current read out during positive bias.

by the scan area of the MEMS mirror and the optical spot size. Our current setup uses a $20\,\mathrm{mm} \times 20\,\mathrm{mm}$ scan area. To ensure independent operation, switches must be separated by some distance. Two FWHMs of the laser spot would give a $4\times$ ratio in the power delivered to two nearby switches, which is likely to be sufficient selectivity. In this case the switch spacing would be approximately $80\,\mu\mathrm{m}$ and there would be $(20,000/80)^2 = 62,500$ addressable locations. The speed at which these switches can be set is determined by the scan speed of the MEMS mirror. The time for each line in the scan is governed by the mirror's resonant frequency ($\approx 1.4\,\mathrm{kHz}$), allowing for a conservative line scan time of $3.6\,\mathrm{ms}$ to traverse the $20\,\mathrm{mm}$ width. For a serpentine scan pattern, stepping between adjacent rows can be accomplished in about $0.5\,\mathrm{ms}$. For an array of 62,500 switches arranged in a $250 \times 250$ grid, the total time to address every switch is: $T_{\mathrm{total}} = 250$ lines $\times$ $(3.6\,\mathrm{ms/line} + 0.5\,\mathrm{ms/step}) \approx 1.03\,\mathrm{s}$. This demonstrates that the entire high-density array can be addressed in approximately one second.

### A. Application to Standard Superconducting Traces

To evaluate the potential of this optical method for a wider variety of materials, we conducted a detailed thermal analysis of a standard $10\,\mu\mathrm{m}$-wide, $50\,\mathrm{nm}$-thick superconducting trace on a silicon substrate. We estimate the deposited power per unit area required to drive the electrons in the trace normal. This is found by numerically solving the 1D steady-state heat equation, which balances lateral heat conduction along the trace, vertical cooling from the trace to the substrate, and the absorbed laser power. The thermal model is adapted from previous work on hotspot formation in superconducting microbridges [28] for the case of optical excitation. The governing equation solved is:

$$-t\frac{d}{dx}\left(\kappa_{\mathrm{e}}(T_{\mathrm{e}})\frac{dT_{\mathrm{e}}}{dx}\right) + g_{\mathrm{eff}}(T_{\mathrm{e}})(T_{\mathrm{e}} - T_{\mathrm{s}}) = I_{\mathrm{abs}}(x), \tag{1}$$

where $T_{\mathrm{e}}(x)$ is the electron temperature profile, $T_{\mathrm{s}} = 20\,\mathrm{mK}$ is the substrate (bath) temperature, $t$ is the film thickness, $I_{\mathrm{abs}}(x)$ is the absorbed laser intensity profile (FWHM $\approx 40\,\mu\mathrm{m}$), and $\kappa_{\mathrm{e}}(T_{\mathrm{e}}) = L_0 T_{\mathrm{e}}/(\rho_{300\ \mathrm{K}}/\mathrm{RRR})$ is the electronic thermal conductivity from the Wiedemann-Franz law, for a material-specific residual-resistance ratio (RRR). For this model, the effective vertical cooling power density can be written as

$$g_{\mathrm{eff}}(T_{\mathrm{e}}) = \frac{\sigma_{\mathrm{K}}(T_{\mathrm{p}}(T_{\mathrm{e}})^4 - T_{\mathrm{s}}^4)}{(T_{\mathrm{e}} - T_{\mathrm{s}})}, \tag{2}$$

where $T_{\mathrm{p}}(T_{\mathrm{e}})$ is the phonon temperature and $\sigma_{\mathrm{K}}$ is the Kapitza boundary conductance between the trace and the silicon substrate [29]. The value of $g_{\mathrm{eff}}(T_{\mathrm{e}})$ is calculated at each point along the trace by solving the two-temperature vertical flux balance between the electrons, phonons, and the substrate given by

$$\Sigma t(T_{\mathrm{e}}^5 - T_{\mathrm{p}}^5) = \sigma_{\mathrm{K}}(T_{\mathrm{p}}^4 - T_{\mathrm{s}}^4), \tag{3}$$

where $\Sigma$ is the electron-phonon coupling constant.

Using this model, we solve (1) numerically to find the incident power required to form a $10\,\mu\mathrm{m}$-long hotspot. The hotspot size ($L$) is chosen to be equal to the wire width ($w$) to model a full quench of the device. This represents an upper limit on the operational power, as in practice a quench occurs as soon as the hotspot is large

TABLE I
COMPARISON OF PERFORMANCE FOR OPTICAL SWITCHING FOR $10\,\mu\mathrm{m}$ WIDE, $50\,\mathrm{nm}$ THICK MO, NB, AND AL TRACES AT $20\,\mathrm{mK}$.

| **Parameter** | **Molybdenum (Mo)** | **Niobium (Nb)** | **Aluminum (Al)** |
|---|---|---|---|
| *Input Material Properties* | | | |
| Critical Temperature ($T_\mathrm{c}$) [K] | 0.91 | 9.3 | 1.3 [30] |
| e-p Coupling ($\Sigma$) [$\mathrm{nW/\mu m^3/K^5}$] | 0.9 [31] | 2.4 [32] | 0.3 [33] |
| Kapitza Conductance ($\sigma_\mathrm{K}$) [$\mathrm{W/m^2/K^4}$] | 500 [34] | 500 [34] | 300 [34] |
| Sommerfeld Constant ($\gamma$) [$\mathrm{mJ/mol/K^2}$] | 2.1 [35] | 7.8 [36] | 1.4 [37] |
| Room-temperature resistivity ($\rho_{300\ \mathrm{K}}$) [$\mu\Omega\cdot\mathrm{cm}$] | 15 [38] | 15 [39] | 1.5 [30] |
| Residual-Resistance Ratio (RRR) | 2 [38] | 6.5 [39] | 2.8 [30] |
| Reflectance at $515\,\mathrm{nm}$ ($R$) | 0.58 [40] | 0.55 [40] | 0.92 [40] |
| *Calculated Metrics* | | | |
| Incident Power ($P_\mathrm{inc}$) [$\mu$W] | 0.18 | $12\times10^3$ | 4.8 |
| Time Constant ($\tau$) [ns] | 340 | 1.1 | 220 |
| Repetition Rate ($f_\mathrm{rep}\approx1/\tau$) [MHz] | 3.0 | 880 | 4.6 |

enough that the remaining superconducting cross-section cannot support the critical current density. The required powers are found to be $0.18\,\mu\mathrm{W}$, $4.8\,\mu\mathrm{W}$, and $12\,\mathrm{mW}$ for Mo, Al, and Nb, respectively.

The results can be understood by examining the relative importance of the individual physical contributions, although the coupled, nonlinear nature of the problem means these effects are not simply additive. The cooling power in the system arises from multiple physical channels that together balance the incident optical heating. For the vertical cooling channels, electron-phonon (e-p) coupling accounts for approximately 24% (13%, 75%) of the total cooling power for Mo (Al, Nb). The acoustic phonon mismatch at the substrate interface provides a comparable contribution of 23% (12%, 24%) in Mo (Al, Nb). In contrast, lateral heat flow, governed by the thermal healing length $\eta\equiv\sqrt{\kappa(T_\mathrm{c})t/g_\mathrm{eff}}$, plays a varied but critical role, with calculated values of $11\,\mu\mathrm{m}$ ($30\,\mu\mathrm{m}$, $0.2\,\mu\mathrm{m}$) for Mo (Al, Nb). Consequently, for Mo and Al, it is the dominant cooling mechanism, accounting for 53% and 75% of the total power dissipation, respectively. For Nb, however, its short healing length results in a minor contribution of just 1%.

Beyond these direct cooling mechanisms, optical factors substantially increase the required incident power. Reflectance losses at the film surface necessitate a power increase of 138% for Mo, 122% for Nb, and 1150% for Al relative to the absorbed power. In future non-prototype devices, anti-reflection coatings will help mitigate this loss. In addition, the mismatch between the Gaussian beam waist ($\approx 34\,\mu\mathrm{m}$) and the healing length requires an additional correction, resulting in a factor of approximately 6.5 (8.7, 5) increase in power for Mo (Al, Nb). The full numerical solution self-consistently balances these competing effects to yield the final required powers.

The device switching speed is characterized by the thermal time constant, $\tau$, which is defined as the ratio of the total heat capacity of the hotspot, $C_\mathrm{HS}$, to its thermal conductance to the substrate, $G_\mathrm{HS}$. The heat capacity is calculated from the volumetric electronic specific heat at the critical temperature, $C_\mathrm{HS}=(\gamma\rho/M)T_\mathrm{c}(w\cdot L\cdot t)$, where $\gamma$ is the Sommerfeld constant, $\rho$ is the mass density, and $M$ is the molar mass. The total conductance represents the cooling efficiency and is the product of the surface area and the effective vertical thermal conductance, $G_\mathrm{HS}=g_\mathrm{eff}(T_\mathrm{c})(w\cdot L)$. The maximum repetition rate is then the inverse of this time constant, $f_\mathrm{rep}\approx1/\tau$.

The results of our calculations, along with the assumed material parameters, are summarized in Table I. A clear trade-off between operational power and device speed emerges from the analysis. Niobium, with its high $T_\mathrm{c}$, exhibits a very short thermal time constant, enabling repetition rates exceeding 800 MHz. This high speed is a direct consequence of the efficient vertical cooling at elevated temperatures, which leads to a large total thermal conductance. However, this performance requires tens of milliwatts of incident power to overcome the powerful cooling channels. In contrast, molybdenum and aluminum are significantly more power-efficient but are consequently two orders of magnitude slower, with reset times in the hundreds of nanoseconds. The lower operating temperatures of these materials result in a smaller thermal conductance and thus a longer cooling time. A key differentiator between these two low-power materials is aluminum's lower resistivity, which is the primary factor contributing to its incident power requirement

being about thirty times that of molybdenum.

## V. Conclusion

We have demonstrated a minimalist, optically-actuated persistent current switch and confirmed its viability for individually addressing elements within an array. By using a scanning laser to locally heat a superconducting segment, we can selectively write and erase persistent currents. While we repurposed thermally isolated TES microcalorimeters for this proof-of-concept, our work establishes a general principle of non-contact thermal switching that is directly compatible with simple, unmodified superconducting traces, eliminating the need for specialized, integrated heater structures.

Our analysis shows that a single cryogenic laser scanner can address a high-density grid of over 60,000 switches within a $20\,\mathrm{mm} \times 20\,\mathrm{mm}$ area in one second. Thermal modeling shows that a simple molybdenum wire switch has a cooling time constant $\tau \approx 300\,\mathrm{ns}$, enabling a theoretical repetition rate over $3\,\mathrm{MHz}$. The combination of individual addressability, scalability, and speed makes optical actuation a powerful and practical architecture for the complex biasing schemes of future cryogenic systems.

## References


[1] J. Clarke and A. I. Braginski, *The SQUID Handbook: Fundamentals and Technology of SQUIDs and SQUID Systems*. Wiley-VCH, 2004. DOI: https://doi.org/10.1002/3527603646.

[2] M. Johnson, P Bunyk, F Maibaum, *et al.*, "A scalable control system for a superconducting adiabatic quantum optimization processor," *Superconductor Science and Technology*, vol. 23, no. 6, p. 065 004, 2010. DOI: https://doi.org/10.1088/0953-2048/23/6/065004.

[3] X Dai, D. Tennant, R Trappen, *et al.*, "Calibration of flux crosstalk in large-scale flux-tunable superconducting quantum circuits," *PRX Quantum*, vol. 2, no. 4, p. 040 313, 2021. DOI: https://doi.org/10.1103/PRXQuantum.2.040313.

[4] S. J. Weber, G. O. Samach, D. Hover, *et al.*, "Coherent coupled qubits for quantum annealing," *Physical Review Applied*, vol. 8, no. 1, p. 014 004, 2017. DOI: https://doi.org/10.1103/PhysRevApplied.8.014004.

[5] S. Khan, B. A. Primavera, J. Chiles, *et al.*, "Superconducting optoelectronic single-photon synapses," *Nature electronics*, vol. 5, no. 10, pp. 650–659, 2022. DOI: https://doi.org/10.1038/s41928-022-00840-9.

[6] S. Kempf, A. Fleischmann, L. Gastaldo, and C. Enss, "Physics and applications of metallic magnetic calorimeters," *Journal of Low Temperature Physics*, vol. 193, no. 3, pp. 365–379, 2018. DOI: https://doi.org/10.1007/s10909-018-1891-6.

[7] C. Schuster and S. Kempf, "SQUID-based superconducting microcalorimeter with in situ tunable gain," *Applied Physics Letters*, vol. 123, no. 25, 2023. DOI: https://doi.org/10.1063/5.0179862.

[8] C. Macklin, K. O'Brien, D. Hover, *et al.*, "A near–quantum-limited josephson traveling-wave parametric amplifier," *Science*, vol. 350, no. 6258, pp. 307–310, 2015. DOI: https://doi.org/10.1126/science.aaa8525.

[9] B. Ho Eom, P. K. Day, H. G. LeDuc, and J. Zmuidzinas, "A wideband, low-noise superconducting amplifier with high dynamic range," *Nature Physics*, vol. 8, no. 8, pp. 623–627, 2012. DOI: https://doi.org/10.1038/nphys2356.

[10] M. Malnou, M. Vissers, J. Wheeler, *et al.*, "Three-wave mixing kinetic inductance traveling-wave amplifier with near-quantum-limited noise performance," *PRX Quantum*, vol. 2, no. 1, p. 010 302, 2021. DOI: https://doi.org/10.1103/PRXQuantum.2.010302.

[11] A Giachero, M Vissers, J Wheeler, *et al.*, "Kinetic inductance traveling wave amplifier designs for practical microwave readout applications," *Journal of Low Temperature Physics*, vol. 215, no. 3, pp. 152–160, 2024. DOI: https://doi.org/10.1007/s10909-024-03078-1.

[12] P. Szypryt, D. A. Bennett, I. Fogarty Florang, *et al.*, "Kinetic inductance current sensor for visible to near-infrared wavelength transition-edge sensor readout," *Communications Engineering*, vol. 3, no. 1, 2024. DOI: https://doi.org/10.1038/s44172-024-00308-y.

[13] L. Longobardi, S. Pottorf, V. Patel, and J. E. Lukens, "Development and testing of a persistent flux bias for qubits," *IEEE transactions on applied superconductivity*, vol. 17, no. 2, pp. 88–89, 2007. DOI: https://doi.org/10.1109/TASC.2007.897413.

[14] H. Deng, Y. Wu, Y. Zheng, *et al.*, "Working point adjustable dc-squid for the readout of gap tunable flux qubit," *IEEE Transactions on Applied Superconductivity*, vol. 25, no. 3, pp. 1–4, 2015. DOI: https://doi.org/10.1109/TASC.2015.2399272.

[15] M. R. Vissers, J. D. Wheeler, P. Szypryt, *et al.*, "In situ frequency tuning of superconducting resonators via nonlinear kinetic inductance," submitted to *Applied Physics Letters*.

[16] L. Testardi, "Destruction of superconductivity by laser light," *Physical Review B*, vol. 4, no. 7,

p. 2189, 1971. DOI: https://doi.org/10.1103/PhysRevB.4.2189.

[17] C. E. Cunningham, B. Cabrera, D. P. Saroff, J. Price, and T. Stevenson, "Low noise switching of a superconducting circuit by a laser induced weak link," *IEEE Transactions on Magnetics*, vol. 25, no. 2, pp. 1022–1025, 1989. DOI: https://doi.org/10.1109/20.92462.

[18] G. S. Park, S. W. Nam, B Cabrera, and M. Huber, "Improved design of an optically switched inductance modulation circuit for noise reduction in SQUID systems," *IEEE Transactions on Applied Superconductivity*, vol. 5, no. 2, pp. 3214–3217, 1995. DOI: https://doi.org/10.1109/77.403275.

[19] C. M. Natarajan, M. G. Tanner, and R. H. Hadfield, "Superconducting nanowire single-photon detectors: Physics and applications," *Superconductor Science and Technology*, vol. 25, no. 6, p. 063 001, 2012. DOI: https://doi.org/10.1088/0953-2048/25/6/063001.

[20] F. Marsili, V. B. Verma, J. A. Stern, *et al.*, "Detecting single infrared photons with 93% system efficiency," *Nature Photonics*, vol. 7, no. 3, pp. 210–214, 2013. DOI: https://doi.org/10.1038/nphoton.2013.13.

[21] R. Ishihara, S. Nur, and J. O. T. Pearl, "Persistent current switch," pat., US Patent App. 18/725,440, 2025. [Online]. Available: https://patents.google.com/patent/WO2023144247A1/en.

[22] K. Stifter, H. Magoon, A. J. Anderson, *et al.*, "Cryogenic optical beam steering for superconducting device calibration," *Journal of Optical Microsystems*, vol. 5, no. 2, pp. 024 503–024 503, 2025. DOI: https://doi.org/10.1117/1.JOM.5.2.024503.

[23] A. Roy, R. Singh, J. C. Weber, *et al.*, "Characterization of Silicon-Membrane TES Microcalorimeters for Large-Format X-ray Spectrometers with Integrated Microwave SQUID Readout," *IEEE Transactions on Applied Superconductivity*, pp. 1–8, 2026. DOI: 10.1109/TASC.2026.3655165.

[24] K. D. Irwin and G. C. Hilton, "Transition-edge sensors," in *Cryogenic particle detection*, Springer, 2005, pp. 63–150. DOI: https://doi.org/10.1007/10933596_3.

[25] J. N. Ullom and D. A. Bennett, "Review of superconducting transition-edge sensors for x-ray and gamma-ray spectroscopy," *Superconductor Science and Technology*, vol. 28, no. 8, p. 084 003, 2015. DOI: https://doi.org/10.1088/0953-2048/28/8/084003.

[26] J. Mates, D. T. Becker, D. A. Bennett, *et al.*, "Simultaneous readout of 128 X-ray and gamma-ray transition-edge microcalorimeters using microwave SQUID multiplexing," *Applied Physics Letters*, vol. 111, no. 6, 2017. DOI: https://doi.org/10.1063/1.4986222.

[27] J. W. Dean, A Roy, N. J. Ortiz, *et al.*, "A laser scanning device for cryogenic beam steering," *IEEE Transactions on Applied Superconductivity*, 2026, to be published in IEEE TAS.

[28] W. Skocpol, M. Beasley, and M Tinkham, "Self-heating hotspots in superconducting thin-film microbridges," *Journal of Applied Physics*, vol. 45, no. 9, pp. 4054–4066, 1974. DOI: https://doi.org/10.1063/1.1663912.

[29] G. L. Pollack, "Kapitza resistance," *Reviews of modern physics*, vol. 41, no. 1, p. 48, 1969. DOI: https://doi.org/10.1103/RevModPhys.41.48.

[30] M Park, K. Lane, J. Parpia, and M. Isaacson, "Modification of aluminum thin films," *Journal of Vacuum Science & Technology A: Vacuum, Surfaces, and Films*, vol. 13, no. 1, pp. 127–131, 1995. DOI: https://doi.org/10.1116/1.579425.

[31] A. Savin, J. P. Pekola, D. Averin, and V. Semenov, "Thermal budget of superconducting digital circuits at subkelvin temperatures," *Journal of applied physics*, vol. 99, no. 8, 2006. DOI: https://doi.org/10.1063/1.2187276.

[32] F. Wellstood, C Urbina, and J. Clarke, "Hot-electron effects in metals," *Physical Review B*, vol. 49, no. 9, p. 5942, 1994. DOI: https://doi.org/10.1103/PhysRevB.49.5942.

[33] M. Meschke, J. Pekola, F. Gay, R. Rapp, and H. Godfrin, "Electron thermalization in metallic islands probed by Coulomb blockade thermometry," *Journal of low temperature physics*, vol. 134, no. 5, pp. 1119–1143, 2004. DOI: https://doi.org/10.1023/B:JOLT.0000016733.75220.5d.

[34] E. T. Swartz and R. O. Pohl, "Thermal boundary resistance," *Reviews of modern physics*, vol. 61, no. 3, p. 605, 1989. DOI: https://doi.org/10.1103/RevModPhys.61.605.

[35] G. K. White and S. Woods, "Electrical and thermal resistivity of the transition elements at low temperatures," *Philosophical Transactions of the Royal Society of London. Series A, Mathematical and Physical Sciences*, vol. 251, no. 995, pp. 273–302, 1959. DOI: https://doi.org/10.1098/rsta.1959.0004.

[36] B. Van Der Hoeven Jr and P. Keesom, "Specific heat of niobium between 0.4 and 4.2 k," *Physical Review*, vol. 134, no. 5A, A1320, 1964. DOI: https://doi.org/10.1103/PhysRev.134.A1320.

[37] N. E. Phillips, "Heat capacity of aluminum between 0.1 K and 4.0 K," *Physical Review*, vol. 114, no. 3, p. 676, 1959. DOI: https://doi.org/10.1103/PhysRev.114.676.

[38] L. Fàbrega, I. Fernández-Martínez, M. Parra-Borderías, *et al.*, "Effects of stress and morphology on the resistivity and critical temperature of room-temperature-sputtered Mo thin films," *IEEE Transactions on applied superconductivity*, vol. 19, no. 6, pp. 3779–3785, 2009. DOI: https://doi.org/10.1109/TASC.2009.2027609.

[39] E. Zikiy, I. Stepanov, S. Bukatin, *et al.*, "Mutual control of critical temperature, residual resistance ratio, stress, and roughness for sputtered Nb films," *Surfaces and Interfaces*, p. 107 266, 2025. DOI: https://doi.org/10.1016/j.surfin.2025.107266.

[40] E. D. Palik, *Handbook of optical constants of solids*. Academic press, 1998, vol. 3.